Journal of Hazardous Materials 193 (2011) 70–81

Contents lists available at ScienceDirect

Journal of Hazardous Materials

journal homepage: www.elsevier.com/locate/jhazmat

Degradation of decabromodiphenyl ether by nano zero-valent iron immobilized in mesoporous silica microspheres

Xinhong Qiu [a], Zhanqiang Fang [a,*], Bin Liang [a], Fenglong Gu [a], Zhencheng Xu [b]

[a] School of Chemistry and Environment, South China Normal University, Guangzhou 510006, China
[b] South China Institute of Environmental Sciences, Guangzhou 510630, China

ARTICLE INFO

Article history:
Received 14 February 2011
Received in revised form 1 July 2011
Accepted 7 July 2011
Available online 18 July 2011

Keywords:
Nano zero-valent iron
Mesoporous silica microspheres
Decabromodiphenyl ether
Nanoparticles

ABSTRACT

The agglomeration of nanoparticles reduces the surface area and reactivity of nano zero-valent iron (NZVI). In this paper, highly dispersive and reactive NZVI immobilized in mesoporous silica microspheres covered with FeOOH was synthesized to form reactive mesoporous silica microspheres (SiO_2@FeOOH@Fe). The characteristics of SiO_2@FeOOH@Fe were analyzed by transmission electron microscopy, Fourier transform infrared spectroscopy simultaneous thermal analysis, X-ray photoelectron spectroscopy, and Brunnaer–Emmett–Teller surface area analysis. The mean particle size of the reactive mesoporous silica microspheres was 450 nm, and its specific surface area was 383.477 $m^2\ g^{-1}$. The degradation of dcabromodiphenyl ether (BDE209) was followed pseudo-first-order kinetics, and the observed reaction rate constant could be improved by increasing the SiO_2@FeOOH@Fe dosage and by decreasing the initial BDE209 concentration. The stability and longevity of the immobilized Fe nanoparticles were evaluated by repeatedly renewing the BDE209 solution in the reactor. The stable degradation of BDE209 by SiO_2@FeOOH@Fe was observed within 10 cycles. Agglomeration-resistance and magnetic separation of SiO_2@FeOOH@Fe were also performed. The improved dispersion of SiO_2@FeOOH@Fe in solution after one-month storage and its good performance in magnetic separation indicated that SiO_2@FeOOH@Fe has the potential to be efficiently applied to environmental remediation.

1. Introduction

Polybromodiphenyl ethers (PBDEs), as efficient flame retardants, have been widely used in electronics, chemicals, electrical, textile and other industries [1,2]. Some studies have been confirmed that PBDEs are ubiquitous persistent organic pollutants in the environment as well as in human and animal bodies [3–5]. The presence of PBDEs in the animal body has been found to affect the balance of thyroid and cause neurotoxicity [6]. Therefore, it is necessary to seek for methods, which have high degradation efficiency and can be used in engineering practice.

Recently, using nanoscale elementary metals, metal oxides, and their composites is a promising method of environmental remediation [7–9]. Compared with zero-valent iron (ZVI), nano zero-valent iron (NZVI) has a larger specific surface area and higher reactivity [10]. NZVI is often used for treating contaminants in aqueous solutions because it could effectively degrade many pollutants, such as organic halogenated hydrocarbons [11,12], nitrates [13], heavy metals [14], insecticides [15], and dyes [16]. And it also showed good reactive ability in BDE209 degradation. In 2010, Shih and Tai [11] reported that the 2.8 mg L^{-1} BDE209 can be rapidly removed by NZVI within 40 min in water solution and the efficiency was much better than that of ZVI. Recently, in our lab, the NZVI was prepared from steel pickling waste liquor and used to remove BDE209 in a water/tetrahydrofuran (4/6, v/v) solution [17]. The results showed that 97.92% of 2 mg L^{-1} BDE209 was removed within 24 h by 4 g L^{-1} NZVI, which was more effective than ZVI under the same conditions.

Aside from its faster reaction rate than ZVI, NZVI can also be directly injected into polluted groundwater and soil, resulting in the immediate degradation of pollutants [18]. However, due to their small size effect and surface effect, NZVI particles are easily aggregated via Van der Waals and magnetic attraction forces, forming particles with diameters ranging from several microns to several millimeters, or even larger in water [19,20]. The agglomeration of these nanoparticles can reduce the surface area and reactivity of NZVI [20,21]. In addition, the poor transport properties of NZVI in aquifers will limit its practical application in the remediation of toxic pollutants in contaminated environments [22].

Two methods are generally adopted to avoid the agglomeration of nanoscale zero-valent iron particles. One is the use of surfactants [23], starches [24], and cellulose [25] to modify the surface of NZVI. By increasing the steric or electrostatic repulsion between particles, nanoscale particles are stabilized and dispersed. The second

* Corresponding author. Tel.: +86 20 39310250; fax: +86 20 39310187.
E-mail addresses: lisan408@yahoo.cn, qbaiyi@qq.com (Z. Fang).

0304-3894/$ – see front matter © 2011 Elsevier B.V. All rights reserved.
doi:10.1016/j.jhazmat.2011.07.024

method involves the embed-immobilization technique, wherein NZVI is loaded onto a functional carrier, such as activated carbon [26,27], a nylon membrane [20,28], or a resin [29]. Radical groups and channels in the carriers can obstruct nanoparticles' clustered. Some carriers can even play certain roles during the degradation process. For instance, Choi et al. [26] developed a new strategy wherein nanoscale Fe was loaded onto activated carbon particles to prepare reactive activated carbon. The particles were avoided to be clustered in the process, and the adsorption capacity for lipophilic pollutants was greatly improved. Recently, the emergence of new materials, such as molecular sieve and silica sphere, which can provide potential carriers to solve the problem of NZVI agglomeration has been attracted interest since they can immobilize various nanoparticles for further applications [19,30]. Meanwhile, surface modification of inorganic core with different inorganic shell to form core–shell structures have shown several applications because these particles show some special properties in optics and catalysis by adjusting their chemical composition and structure order recently [31,32]. Since the good thermal and chemical stability, non-toxicity, and biocompatible capacity, silica spheres are widely used in fabricating core–shell for further application [33,34]. For example, Shen et al. [34] prepared and demonstrated the h-SiO_2/TiO_2 core/shell microspheres have significant photocatalytic activity in degradation of methyl orange in water. Unfortunately, reports on the preparation and application of composite functional materials with NZVI immobilized in mesoporous silica microspheres or other new carriers are limited, let alone using NZVI immobilized onto mesoporous silica spheres to form core–shell structure to remove toxic organic pollutants.

Hence, a new synthesis method was used to prepare reactive mesoporous silica microspheres with a core–shell structure in this study. Transmission electron microscopy (TEM), X-ray photoelectron spectroscopy (XPS) and temperature-programmed reduction (TPR) were applied to analyze and characterize the material. BDE209 was selected as the contaminant to be removed to study the degradation capacity of the new composite material. The longevity and anti-agglomeration capacity of the composites were also tested.

2. Experimental

2.1. Materials

A standard solution of decabromodiphenyl ether was purchased from Cambridge Isotope Laboratories (CIL, Andover, U.S.) and used to establish the standard curve. Decabromodiphenyl ether (98%, AR grade) was purchased from Aladdin (Shanghai, China) and used as the degradation sample. Ferrous sulfate ($FeSO_4{\cdot}7H_2O$, >99%), sodium borohydride ($NaBH_4$ > 98%), PEG, and ethanol (EtOH, 99.7%) were supplied by Tianjin Damao Chemical Agent Company (Tianjin, China). Tetraethoxysilane and dodecylamine were purchased from Aladdin (Shanghai, China). Methanol (HPLC grade) was supplied by Tianjin Kermel Chemical Reagents Company.

2.2. Synthesis of materials

2.2.1. Preparation of mesoporous silica microspheres

The synthesis of mesoporous silica microspheres was performed according to the method of Miyaka et al. [35]. The main synthesis steps were as follows: About 0.2224 g of dodecylamine was dissolved in EtOH (62.5 vol%) under magnetic stirring in a 50 mL conical flask. Then, 1.16 mL of undiluted liquid tetraethoxysilane were slowly dropped into the solution, which was then stirred for 30 s and allowed to stand for 3 h under room temperature. The products were separated by centrifugation (centrifugation speed, 4000 rpm; time, 10 min) and rinsed with water and EtOH. Afterwards, the products were kept in a vacuum drying chamber for 4 h at 60 °C, heated in a muffle furnace up to 600 °C at a rate of 10 °C min^{-1}, and maintained for 4 h to remove the organic template under high temperature calcination. To regenerate the OH^- groups lost from the surface of SiO_2 during calcination, the silica microspheres were boiled in water for 2 h [36], and then dried in a drying chamber at 60 °C after centrifugation.

2.2.2. Coating the mesoporous silica microspheres with FeOOH

About 0.5 g $FeSO_4{\cdot}7H_2O$ was added to a 50 mL solution containing 0.5 g PEG. The solution was then treated via ultrasonic vibration for 15 min for complete dissociation. About 0.5 g boiled silica spheres was immersed in the solution for 30 min. The pH of the solution as this time was 4.85. Afterwards, the particles were removed and placed in a drying chamber for 3 h at 110 °C. The dried particles were flushed with water and EtOH and then dried in a vacuum drying chamber for 4 h at 60 °C. This produced silica microspheres covered with FeOOH, presented as SiO_2@FeOOH.

2.2.3. Synthesis of reactive mesoporous silica microspheres

About 0.2 g SiO_2@FeOOH was put into three flasks, after which 50 mL EtOH (30 vol%) containing 0.2 g $FeSO_4{\cdot}7H_2O$ was added. The solution was stirred well. Then, 20 mL EtOH (30 vol%) with 0.16 g $NaBH_4$ was added drop-wise while stirring continuously for 10 min. The solution system turned from yellow to black. The products were separated by vacuum filtration and then separately rinsed thrice with water and EtOH. The products were then placed in a drying chamber at 60 °C. Reactive mesoporous silica microspheres, SiO_2@FeOOH@Fe, with core–shell structures were obtained. The overall process of SiO_2@FeOOH@Fe synthesis is shown in Fig. 1. Meanwhile, in order to study the effect of FeOOH on degradation efficiency, the SiO_2@ Fe was also prepared as well as SiO_2@FeOOH@Fe but used SiO_2 as a carrier.

To compare the degradation efficiency of the new synthetic material and NZVI on BDE209, NZVI was synthesized according to previous literature [37]. Briefly, EtOH (30 vol%) was used to prepare 0.2 g L^{-1} $FeSO_4{\cdot}7H_2O$ and 0.16 g L^{-1} $NaBH_4$. Under mechanical stirring, the $NaBH_4$ aqueous solution was added to $FeSO_4{\cdot}7H_2O$; the resulting solution was continuously stirred until it turned black. The particles were separated by vacuum filtration, and separately rinsed thrice with deoxygenated water and EtOH. Finally, the particles were stored in a vacuum drying chamber until further use.

2.3. Characterization

TEM (TECNAI 10, PHILIPS, The Netherlands) was used to observe the size and morphology of the particles. Thermogravimetric and differential thermal simultaneous analyses (STA 409 PC/4/H, NETZSCH, Germany) were performed in the atmosphere from room temperature to 800 °C at a heating rate of 10 °C min^{-1}. Particle surface elemental analysis was performed using XPS (ESCALAB 250, Thermo-VG Scientific, USA) with light as the mono Al Kα (energy: 1486.6 eV, scan mode: CAE, full spectrum scan: pass energy of 150 eV, narrow spectrum scan: pass energy of 20 eV). The crystalline phase of different particles was determined using an X-ray diffractometer (Y-2000, Dandong, China) with a Cu Kα radiation. The accelerating voltage and applied current were 30 kV and 20 mA, respectively. FT-IR spectra of SiO_2@FeOOH and SiO_2 was recorded on a IR-prespige-21 spectrometer (Shimadzu, Japan). The specific surface area and porosity were measured by an ASAP2020M instrument (Micromeritics Instrument Corp, USA). Fe content was measured by an inductively coupled plasma (ICP) optical emission spectrometer (IRIS Intrepid II XSP, Thermo Elemental Company, USA).

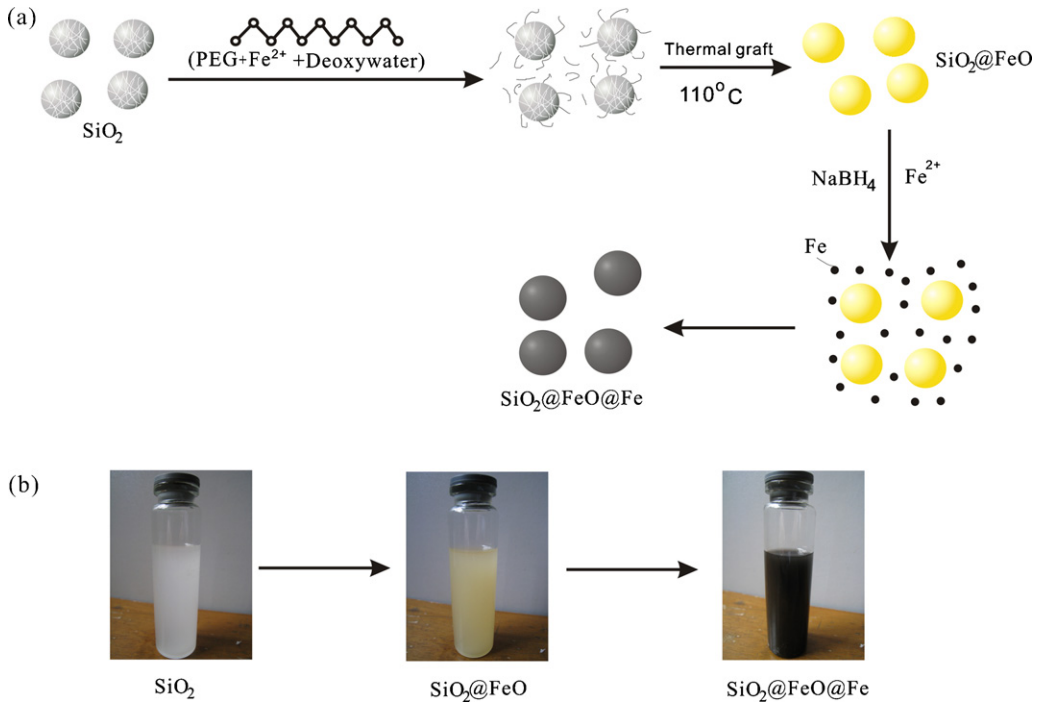

Fig. 1. (a) Schematic illustration of immobilization of nano zero-valent iron nanoparticles on mesopourous silica microspheres, (b) photograph of SiO_2, SiO_2@FeOOH, and SiO_2@FeOOH@Fe.

2.4. Degradation of BDE 209 by SiO_2@FeOOH@Fe

2.4.1. Preparation of the BDE209 solution

BDE209 with high hydrophobicity is difficult to dissolve in water [38,39]. To verify the feasibility of using the new method to remove the BDE209 from a solution, many researchers choose organic solvents (e.g., tetrahydrofuran (THF) [40], methane [41], and acetonitrile [42]) in their experiments. Therefore, the stock solution (100 mg L^{-1}) of BDE209 was made using pure THF as the solvent. A BDE209-simulated solution with the desired concentration was prepared by spiking a known volume of the stock solution with a certain proportion of the THF/water (v/v) solution, such as 4/6, 8/2, 7/3 and pure THF.

2.4.2. Batch experimental procedure

Batch degradation tests were performed in a 10 mL glass tube with a plug. For each batch, certain particles were added to the tubes, after each 10 mL of the stimulated BDE209 solution at a certain concentration were added. The tubes were placed in an oscillator with a speed of 200 rpm at room temperature and then plugged with polytetrafluoroethylene. One of the tubes was removed at each interval, and the solution was extracted with a syringe. The extracted solution was filtered through a 0.45 μm filtration membrane, and the BDE209 concentration was tested by liquid chromatography. Parallel experiments were followed the same procedures above. Control experiments were also performed without particles.

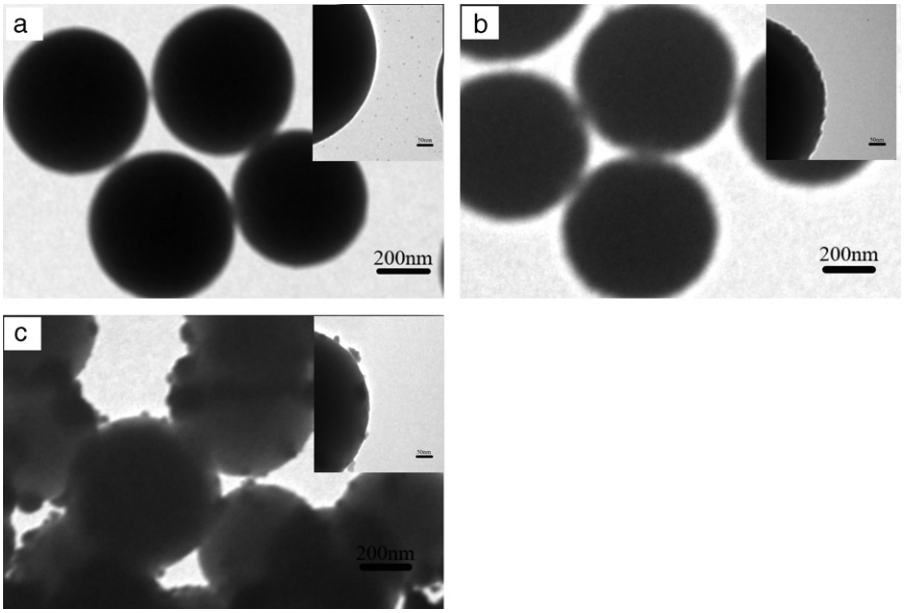

Fig. 2. TEM images of (a) SiO_2, (b) SiO_2@FeOOH, and (c) SiO_2@FeOOH@Fe. The insets show the blowup TEM images of one sphere surface.

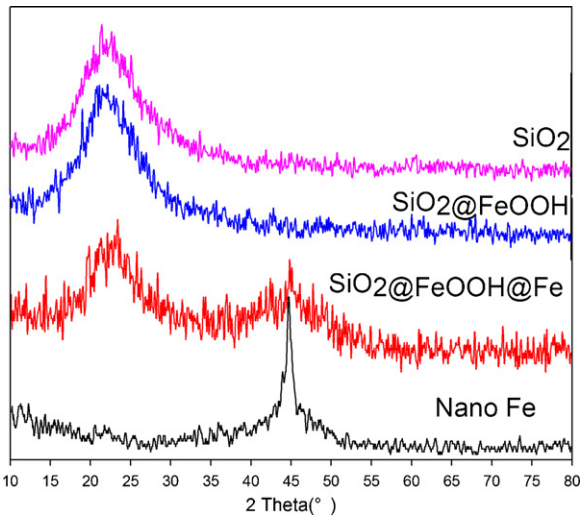

Fig. 3. XRD pattern of SiO_2, SiO_2@FeOOH, SiO_2@FeOOH@Fe and NZVI.

2.5. Analysis methods

The concentration of BDE209 in these samples was determined by HPLC (Shimadzu, LC10A HPLC) with a UV detector (SPD-10AV) at 240 nm. A Dikma C18 column (250 mm × 4.6 mm) was used. The mobile phase was 100% methanol delivered at a rate of 1.2 mL min^{-1}. Each sample size was 20 μL. Quantification was done with a calibration curve of the BDE209 standard.

3. Results and discussion

3.1. Characterization of synthetic material

TEM photographs for SiO_2, SiO_2@FeOOH, and SiO_2@FeOOH@Fe are shown in Fig. 2. Fig. 2a shows that the mesoporous silica microspheres synthesized by dodecylamine and tetraethoxysilane were uniform in size with an average diameter of 450 nm. The edges of the silica microspheres were observed under higher magnification, and their surface was observed to be smooth in the absence of modification (Fig. 2a).

When coated with an FeOOH layer, the sizes of the particles did not significantly change, but their surface became rough with an abundance of embossed points (Fig. 2b) and more –OH was brought by FeOOH layer may enhance the electronegativity of mesoporous silica microspheres. In the solution system containing 30% ethanol (the solution used in the synthetic process), the zeta electric potential of the mesoporous silica microsphere of unmodified FeOOH was −15.78 mV, while the one of modified FeOOH was −25.78 mV. Due to the zeta electric potential of nano zero-valence iron particle of +5.21 mV, the silica microsphere of modified FeOOH can provide a better electric charge environment of the surface to realize a better combination with the particle.

Fig. 2c shows mesoporous silica microspheres loaded with NZVI. A number of small particles within 100 nm were attached to the surface of the microspheres; these particles were determined to be NVZI. Most of NZVI existed in the exterior of mesoporous silica microspheres because the size of nano zero-valent iron and formed protruding points, which can facilitate contact and reaction with pollutants.

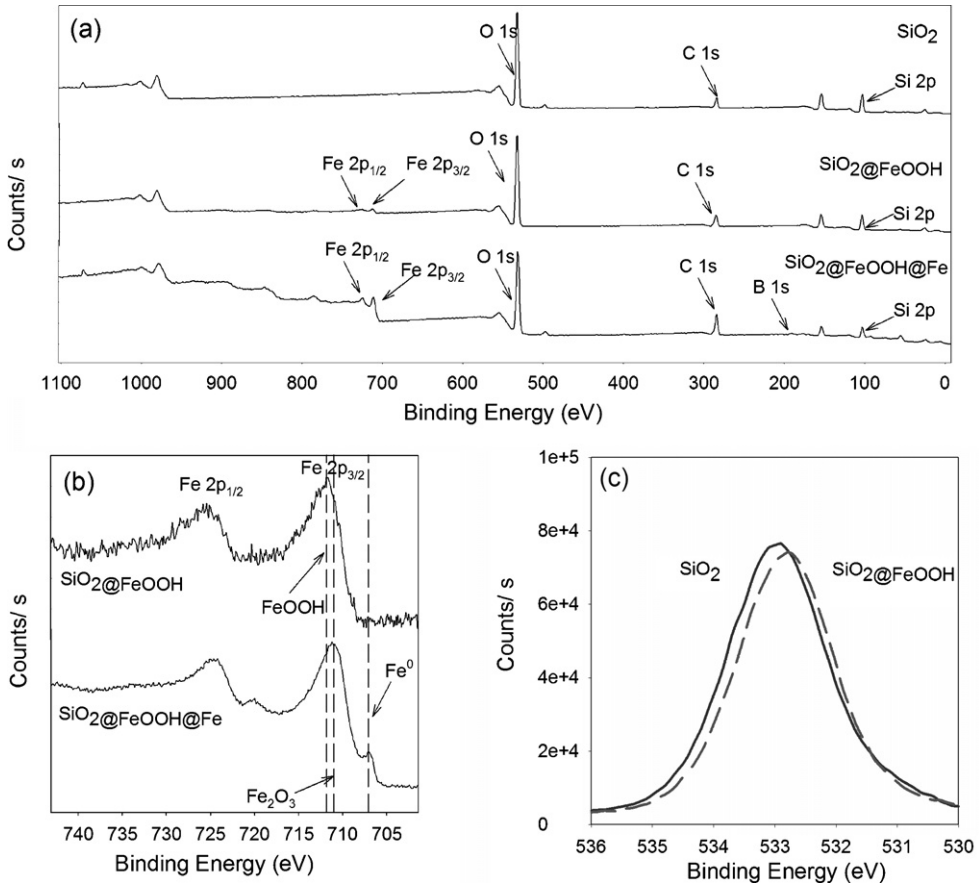

Fig. 4. (a) XPS spectra of SiO_2, SiO_2@FeOOH, and SiO_2@FeOOH@Fe, (b) XPS spectrum for the narrow scan of Fe 2p on the surface of SiO_2@FeOOH and SiO_2@FeOOH@Fe, (c) XPS spectrum for the narrow scan of O 1s on the surface of SiO_2, SiO_2@FeOOH.

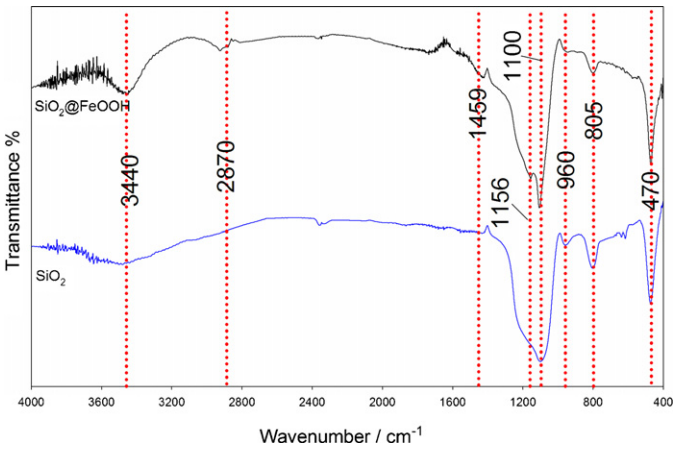

Fig. 5. FT-IR of SiO_2 and SiO_2@FeOOH.

The XRD pattern of the synthesized particles is shown in Fig. 3. From the Fig. 3, except the characteristic diffraction peaks of silica and composite silica at 28° and peaks of zero-valent iron at 44°, we can see that no other peak like oxide iron appeared in the XRD graph. This may be caused by the rare contents of iron oxide. Therefore, XPS was further introduced to study the surface chemical compositions. Results from XPS analysis are shown in Fig. 4. From the full spectrum scan (Fig. 4a), significant Fe 2p binding energy peaks are found on the surface of SiO_2@FeOOH and SiO_2@FeOOH@Fe compared with SiO_2 (Si 2p, C 1s, and O 1s). B 1s binding energy peak on the surface of SiO_2@FeOOH@Fe was produced due to the reduction between $NaBH_4$ and the Fe ions. Fig. 4b shows Fe 2p of SiO_2@FeOOH and SiO_2@FeOOH@Fe, where the 711.5 eV binding energy of Fe 2p in SiO_2@FeOOH corresponded to that of FeOOH [43,44], indicating that the Fe in the second layer existed in the form of FeOOH. In the spectrogram of Fe 2p of SiO_2@FeOOH@Fe, binding energies of 706.9 and 710.8 eV corresponded to the ZVI and Fe oxidation states (Fe_2O_3), respectively. This indicates that the NZVI particles are covered with an oxide film. This film could have been generated during the preparation process. The characteristic peak of O in the Si–O bond at 1s (Fig. 3c) shifted from 532.8 (SiO_2 curve) to 531.1 eV (SiO_2@FeOOH), indicating a shift to lower energy because Si–O–H turned to Si–O–C after PEG was grafted by SiO_2 to the surface of the spheres. C has a larger electro-negativity than H (H: 220, C: 245), thus the characteristic peak shifted to lower energy levels. However, due to the electron donating effect of the Si–O-linked alkyl, the surface charge density of the Si and O atoms increased, which enhanced the shielding effects on the 2p electron of the Si atom and the 1s electron of the O atom. Consequently, the binding energies of the 2p electron of the Si atom and the 1s electron of the O atom were weakened, proving that PEG chains were incorporated into SiO_2 [45]. In order to further confirm the PEG was successfully grafted to SiO2, infrared spectroscopy of SiO_2 and SiO_2@FeOOH has been carried out. As shown in the Fig. 5, there was a wide and large absorption band within the wave number of 3440 cm^{-1}, which mainly caused by the adsorbed water on the surface and the stretching vibration of O–H in the Si–OH. Meanwhile, the absorption peak at 805 cm^{-1} and 470 cm^{-1} was caused by the symmetric stretching vibration of Si–O–Si. In addition, the absorption peak at 960 cm^{-1} was caused by the bending vibration of Si–OH on the surface of silica microsphere. While as for SiO_2@FeOOH, except the characterization band of SiO_2, there are still the C–H absorption peaks at 2870 cm^{-1}, as well as the C–H absorption peak 1459 cm^{-1}. The C–O–Si stretching vibration peak also appeared at the 1156 cm^{-1}. Combined with the TGA results we discussed in the manuscript, these all showed that the PEG was successfully grafted to SiO_2.

Table 1
Specific surface area and porosimetry of different particles.

	BET ($m^2\ g^{-1}$)	Average pore diameter (nm)	Particle size (nm)
NZVI	35.6962	11.548	50–80
SiO_2	543.3220	2.1098	400–500
SiO_2@FeOOH	130.9155	2.1627	400–500
SiO_2@FeOOH@Fe	383.4766	2.1704	400–500

Fig. 6 shows the simultaneous thermal analysis of SiO_2, SiO_2@FeOOH, and SiO_2@FeOOH@Fe. In the differential scanning calorimetry curves for these three materials, endothermic peaks at 85.1, 83.6, and 83.9 °C, representing the evaporation of water, corresponded to weight loss rates of 8.34%, 7.36%, and 6.31%, respectively. The quality of the elemental silica microspheres did not vary significantly as the temperature increased. However, several evident changes for SiO_2@FeOOH and SiO_2@FeOOH@Fe were observed. The qualities of these compounds significantly changed when the temperature increased from 160 to near 340 °C, mainly due to the dehydration of FeOOH to Fe_2O_3 and carbonization of PEG. The exothermic peaks that appeared at 277.6 and 310.7 °C were caused by the combustion of PEG. The nanoscale particles on the surface appeared to play a hindering role, and the burning temperature of PEG for SiO_2@FeOOH@Fe was higher than that for SiO_2@FeOOH. The appearance of the combustion peak proves that PEG was grafted onto the microspheres. The quality of the SiO_2@FeOOH materials continued to decline, probably due to OH^- losses in the Fe_2O_3 structure when FeOOH was completely converted to Fe_2O_3. The weight of SiO_2@FeOOH@Fe started to increase between 400 and 500 °C, and an apparent exothermic peak was generated at 439.9 °C. These may have been caused by the conversion of NZVI to Fe_2O_3 by combustion. The results here are consistent with those obtained for the thermoanalysis of NZVI by Ponder et al. [46]. Because surface layer of nano zero-valent iron was formed during the preparation. And that iron oxide layer cover on the surface of nano zero-valent iron effectively delayed oxidation of inner zero-valent iron during the simultaneous thermal analysis.

Fig. 7 shows the nitrogen adsorption–desorption isotherms of SiO_2, SiO_2@FeOOH and SiO_2@FeOOH@Fe. The nitrogen adsorption isotherm is similar to that of Miyake et al. [35] and Araki et al. [47], which is type IV nitrogen adsorption–desorption isotherms according to the IUPAC classification and showed features of mesoporous materials. The specific surface area of silica oxide was 543.322 $m^2\ g^{-1}$, as measured by the nitrogen adsorption–desorption method, indicating that the material has a large specific surface area. The average pore diameter was 2.11 nm, indicating that the microsphere has a mesoporous structure. This also indicted by the small-angel XRD pattern of the prepared SiO_2 microspheres. As shown in Fig. S1 (see Supplementary data), a single broad XRD peak was observed at around 2.8–2.2° means that some order pore structure exists in the sample. Moreover, combined with the HRTEM image of mesoporous silica microspheres (Fig. S2, see Supplementary data) and some reports [47], the sphere we synthesized contained pore and the nanostructure may be a wormhole-like pore structure. However, the specific surface area decreased after the spheres were covered with a FeOOH film (loading weight ratio of the Fe particle is 1.8% as measured by ICP). The specific surface area decreased to about 130.916 $m^2\ g^{-1}$. After loading the NZVI, the specific surface area of the spheres became 383.477 $m^2\ g^{-1}$. Although this specific surface area was lower than that of pure silica oxides, it was still higher than that of NZVI (35 $m^2\ g^{-1}$). The ICP results indicate that the mass of Fe account of 18.01% of those of the microsphere composites. The BET specific surface area and average pore diameter are summarized in Table 1.

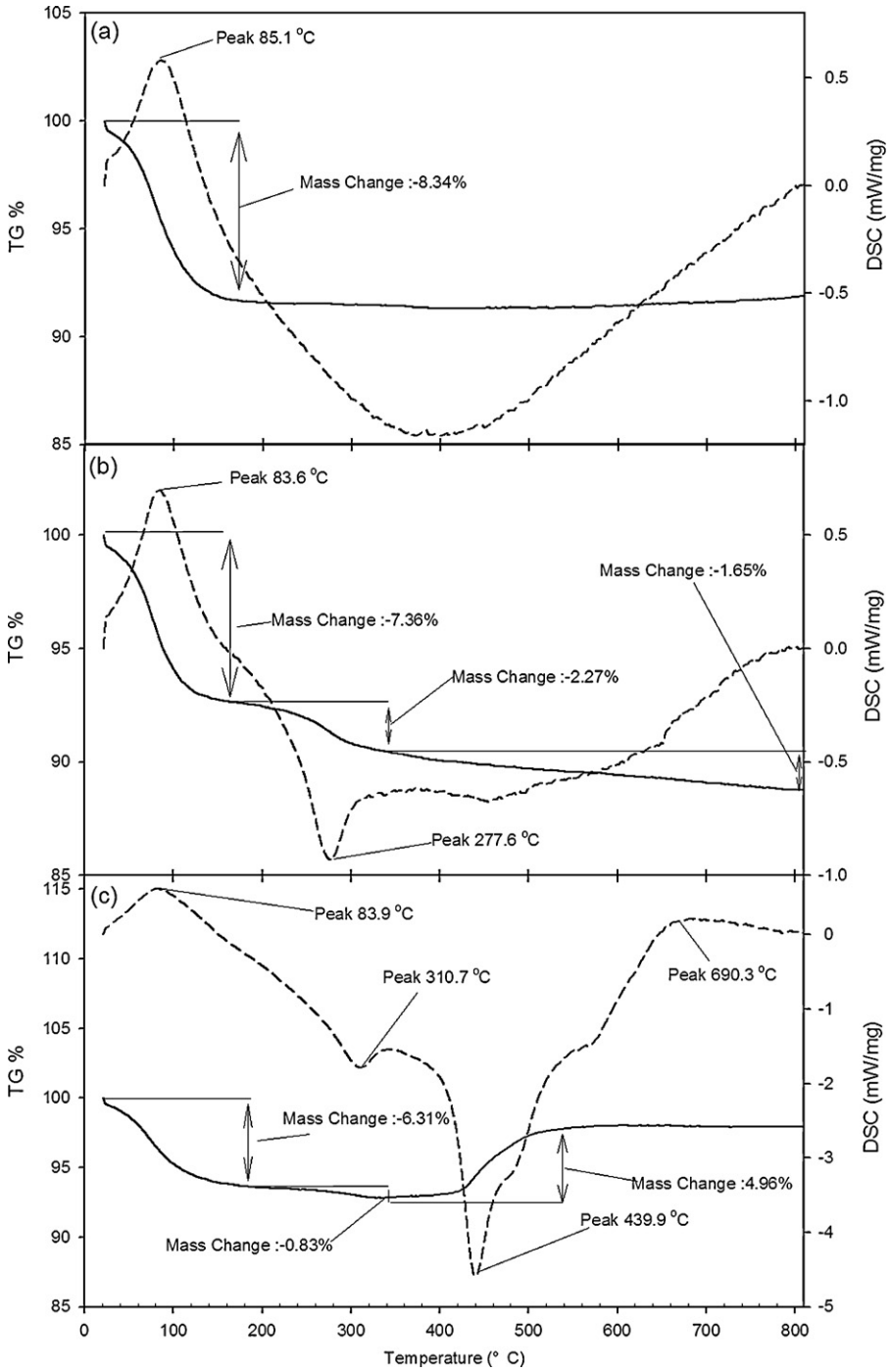

Fig. 6. Thermoanalysis of (a) SiO_2, (b) SiO_2@FeOOH, and (c) SiO_2@FeOOH@Fe.

3.2. The effect of FeOOH on degradation

As shown in the Fig. 8, it is clearly showed that the degradation effectively of BDE209 by SiO_2@FeOOH@Fe was faster than SiO_2@Fe. At the end of reaction, near 100% of BDE209 have been removed by SiO_2@FeOOH@Fe, but 65.48% for the SiO_2@Fe. The reason can be the existence of FeOOH layer in SiO_2@FeOOH@Fe provided more adsorption sites to facilitate the absorption of pollutant. So the silica microsphere, having modified FeOOH, has better removal efficiency than unmodified one during the reaction process.

3.3. Comparison of the degradation efficiency by different particles

Fig. 9a shows the degradation efficiency of BDE209 over time by different particles. Under the same quality of NZVI, 39.36% of the BDE209 was removed by the nano Fe during 8 h of oscillation, whereas 94.15% of the BDE209 was removed in 8 h by SiO_2@FeOOH@Fe. This shows that SiO_2@FeOOH@Fe presents superior degradation efficiency compared with nano Fe. Previous reports showed that organic halogenated contaminants are

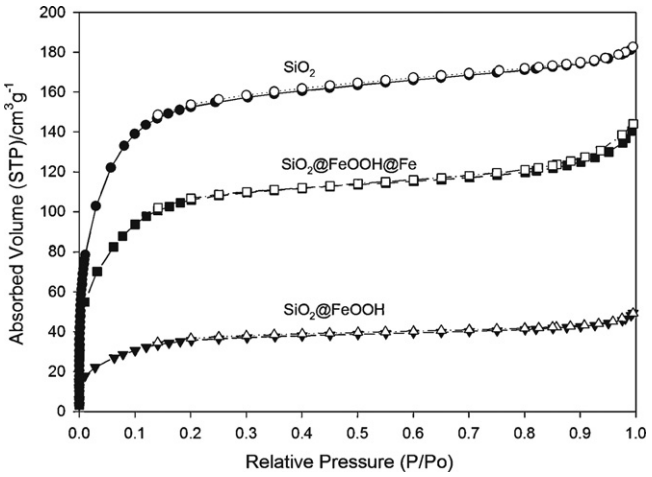

Fig. 7. Nitrogen adsorption/desorption isotherms of SiO_2, SiO_2@FeOOH, and SiO_2@FeOOH@Fe.

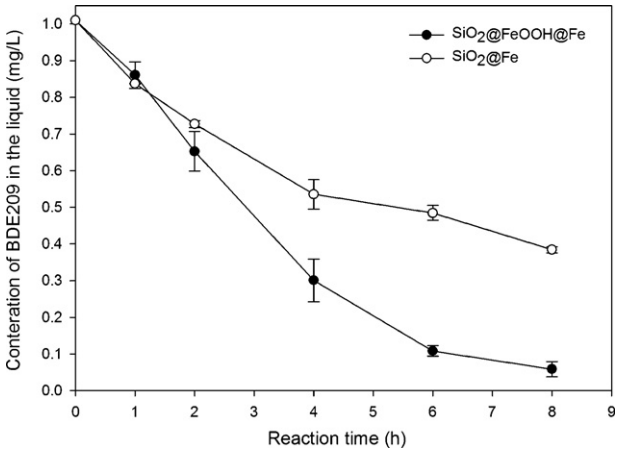

Fig. 8. Effect of FeOOH on the debromination efficiency. (Fe loading of SiO_2@FeOOH@Fe and SiO_2@Fe were 3.96 g L^{-1}; initial concentration of BDE209, 1 mg L^{-1}; reaction time, 8 h; temperature, 28 ± 2 °C; and pH 6.09.)

removed by ZVI through a hydrogenation and debromination process. This process can be expressed by the following Eqs. (1)–(3) [48–50]: (X = Cl, Br):

$$Fe^0 \rightarrow Fe^{2+} + 2e^- \quad (1)$$

$$C_xH_yX_z + zH^+ + ze^- \rightarrow C_xH_{y+z} + zX^- \quad (2)$$

$$2Fe^{2+} + RX + H^+ \rightarrow 2Fe^{3+} + RH^+X^- \quad (3)$$

From these equations, H ions in the solution will be consumed in the reaction, resulting in increases in pH and Fe ions until equilibrium is reached. At equilibrium, the Fe ions will react with OH^- and then begin to precipitate. Therefore, the concentration of Fe ions and pH can approximately reflect the reaction rate during its early stages. The concentrations of Fe ions and pH changed over time during the reactions of nanoscale Fe and SiO_2@FeOOH@Fe (Fig. 9b). Comparing the reaction systems, the concentration of Fe ions and pH of SiO_2@FeOOH@Fe were significantly higher than those of the nanoscale Fe, indicating that SiO_2@FeOOH@Fe was more reactive. In addition, the kinetics of BDE209 removal by SiO_2@FeOOH@Fe and NZVI can be calculated by the equation, which is the expression of Langmuir–Hinshelwood kinetics model and also called the pseudo first-order model [51]:

$$\ln \frac{c_t}{c_0} = -k_{obs}t \quad (4)$$

where c_t is the concentration of BDE209 at selected times (mg L^{-1}); c_0 is the initial BDE209 concentration (mg L^{-1}); k_{obs} is the observed rate constant (h^{-1}); and t is time (h). The observed reaction rate constant (k_{obs}) values were calculated by the method of linear regression. The rate constants of the nanoscale Fe and SiO_2@FeOOH@Fe obtained from Eq. (4) were 0.0569 h^{-1} and 0.3974 h^{-1}, respectively. The rate constant of SiO_2@FeOOH@Fe was 6.9 times greater than that of NZVI. The degradation process of NZVI is a surface reaction. In addition to the good dispersion of SiO_2 in water, SiO_2@FeOOH@Fe is more likely than NZVI to be exposed to BDE209 in the absence of a carrier and a stabilizer. This difference in dispersibility can be shown by the sedimentation experiments. As seen in Fig. S3 (see Supplementary data), most of the NZVI settled at the bottom of the colorimeter tube after 8 min, whereas SiO_2@FeOOH@Fe remained dispersed in the solution. This was because NZVI is prone to forming large particles by agglomeration, leading to a decline in its specific surface area and eventually reducing its dispersibility and reactivity. However, when NZVI is loaded onto the surface of SiO_2@FeOOH, the particles become more dispersed and difficult to coacervate due to the existence of a carrier, resulting in higher dispersibility and reactivity.

Both SiO_2@FeOOH and SiO_2 have high specific surface areas. However, their removal efficiencies within 8 h were 25.12% and 17.08%, respectively. Although the results show that SiO_2 covered with FeOOH layer can improve the removal efficiency of BDE209, both of them are not as efficient as the removal efficiencies of reactive nanoscale materials since SiO_2@FeOOH and SiO_2 lack ability

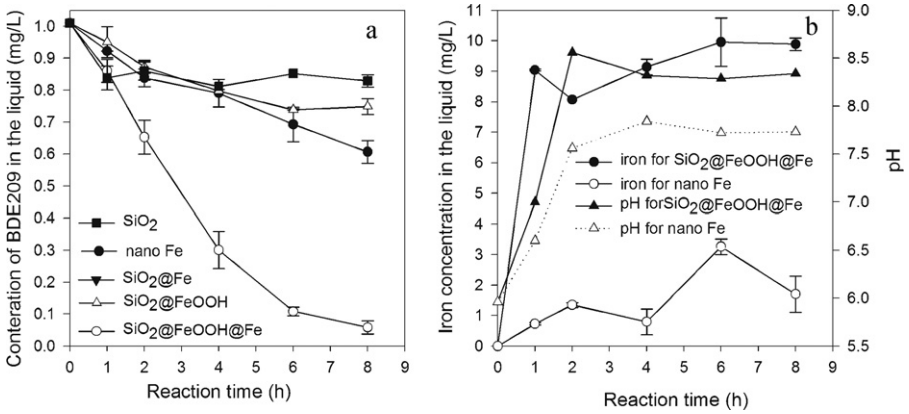

Fig. 9. (a) Comparison of BDE209 degradation by NZVI, SiO_2, SiO_2@FeOOH, and SiO_2@FeOOH@Fe. (b) Concentration of iron ion and pH value of NZVI and SiO_2@FeOOH@Fe. (NZVI addition, 4 g L^{-1}; SiO_2, SiO_2@FeOOH, and SiO_2@FeOOH@Fe addition, 22 g L^{-1}. Fe loading of SiO_2@FeOOH@Fe was 18.01 wt%; initial concentration of BDE209, 1 mg L^{-1}; reaction time, 8 h; temperature, 28 ± 2 °C; and pH 6.09.)

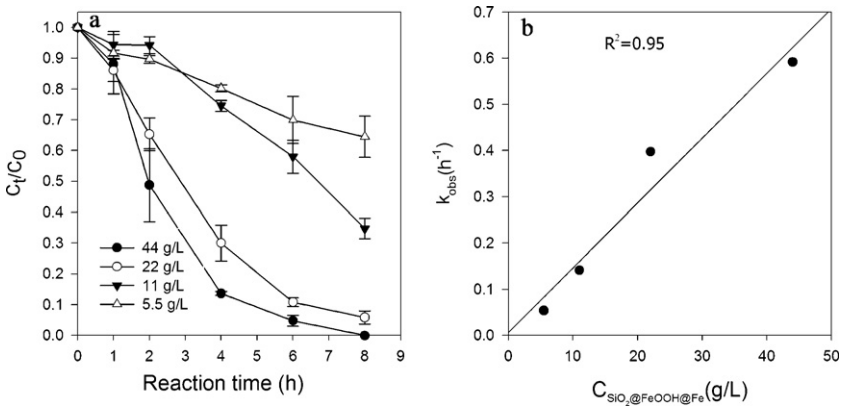

Fig. 10. (a) Effect of SiO_2@FeOOH@Fe addition on the degradation efficiency; (b) relationship of observed rate constant and the addition of SiO_2@FeOOH@Fe. (Fe loading of SiO_2@FeOOH@Fe was 18.01 wt%; initial concentration of BDE209, 1 mg L^{-1}; reaction time, 8 h; temperature, 28 ± 2 °C; and pH 6.09.)

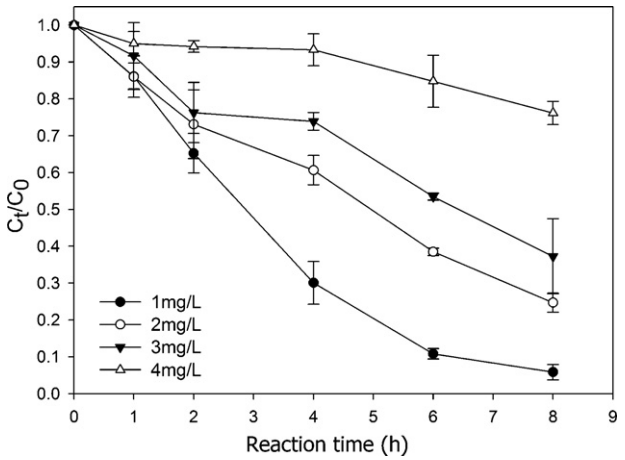

Fig. 11. Effect of the initial concentration on the degradation efficiency. (SiO_2@FeOOH@Fe addition, 22 g L^{-1}. Fe loading of SiO_2@FeOOH@Fe was 18.01 wt%; reaction time, 8 h; temperature, 28 ± 2 °C; and pH 6.09.)

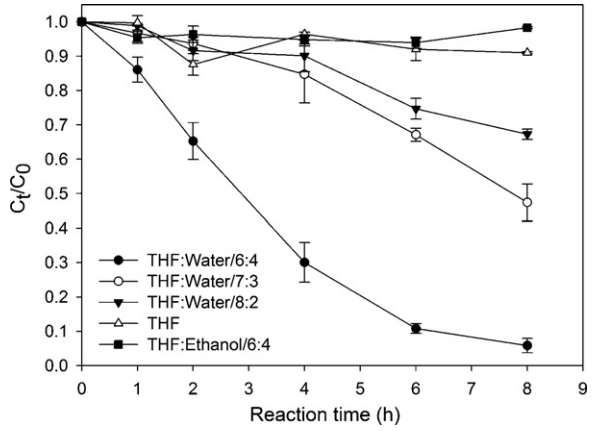

Fig. 12. Effect of solvent conditions on the BDE209 degradation efficiency. (SiO_2@FeOOH@Fe addition, 22 g L^{-1}, Fe loading of SiO_2@FeOOH@Fe was 18.01 wt%; initial concentration of BDE209, 1 mg L^{-1}; reaction time, 8 h, temperature, 28 ± 2 °C.)

of degradation. And these results also reflect that the adsorption capacity of SiO_2 to BDE209 is weak.

3.4. Effect of SiO_2@FeOOH@Fe particle addition

As shown in Fig. 10, the degradation efficiencies within 8 h are 100%, 94.15%, 65.24%, and 35.51% for 44, 22, 11 and 5.5 g L^{-1} of SiO_2@FeOOH@Fe particle addition, respectively. The degradation efficiency of BDE209 was improved with increasing SiO_2@FeOOH@Fe dosages. The same pattern was reflected by the reaction rate constants obtained, which were 0.5917, 0.3974, 0.1413, and 0.0538 h^{-1} for 44, 22, 11, and 5.5 g L^{-1} of particle addition, respectively. When the data were plotted as the observed rate constant (k_{obs}) against the mass loading of SiO_2@FeOOH@Fe, a linear regression equation can be found in Fig. 10b, and the correlation coefficient (R^2) of this line is 0.95, which clearly showed that the observed rate constant (k_{obs}) is proportional to the mass loading of SiO_2@FeOOH@Fe and k_{obs} can be improved by increasing the SiO_2@FeOOH@Fe particle addition. This because the degradation of BDE209 by SiO_2@FeOOH@Fe can be described by the Langmuir–Hinshelwood mode, which suggests that the degradation process is occurred on the surface of the nanoscale metal and the surface reaction is the control step. Therefore, the surface area is an important factor for removing pollutants. The larger the surface area is, the larger the number of reaction sites, resulting in better adsorption and degradation capacity. Thus, increasing the dosage of nanoscale metals results in the provision of more reaction sites, leading to improved degradation efficiency [10,52].

3.5. Effect of initial BDE209 concentration

Given that the concentration of SiO_2@FeOOH@Fe was fixed at 22 g L^{-1} at a steady reaction temperature of 28 ± 2 °C and that the initial concentrations of BDE209 were varied to 1, 2, 3, and 4 mg L^{-1}, the relationship between the reaction time with different initial BDE209 concentrations and degradation efficiencies is illustrated in Fig. 11. After 8 h, the degradation rates were 94.15%, 75.3%, 62.73%, and 34.73% for the initial BDE209 concentrations of 1, 2, 3, and 4 mg L^{-1}, respectively. As the initial concentration increased, the reaction rate constant gradually decreased from 0.3974 h^{-1} at 1 mg L^{-1} to 0.0492 h^{-1} at 4 mg L^{-1}. The degradation of BDE209 by SiO_2@FeOOH@Fe is an interface reaction, the rate determining step is surface reaction. When kept the same mass loading of SiO_2@FeOOH@Fe, with the more of pollutant concentration, the more degradation products of BDE209 on the surface of the material may occupy for reaction sites or compete with the BDE209 for reaction sites, thus affecting the degradation of BDE209 and causing the decline in the reaction rate of BDE209.

3.6. Effect of solvent properties on degradation efficiency

To demonstrate the importance of protons in removing BDE209, degradation experiments were performed in different solvent systems. The influence of different solvent systems on BDE209

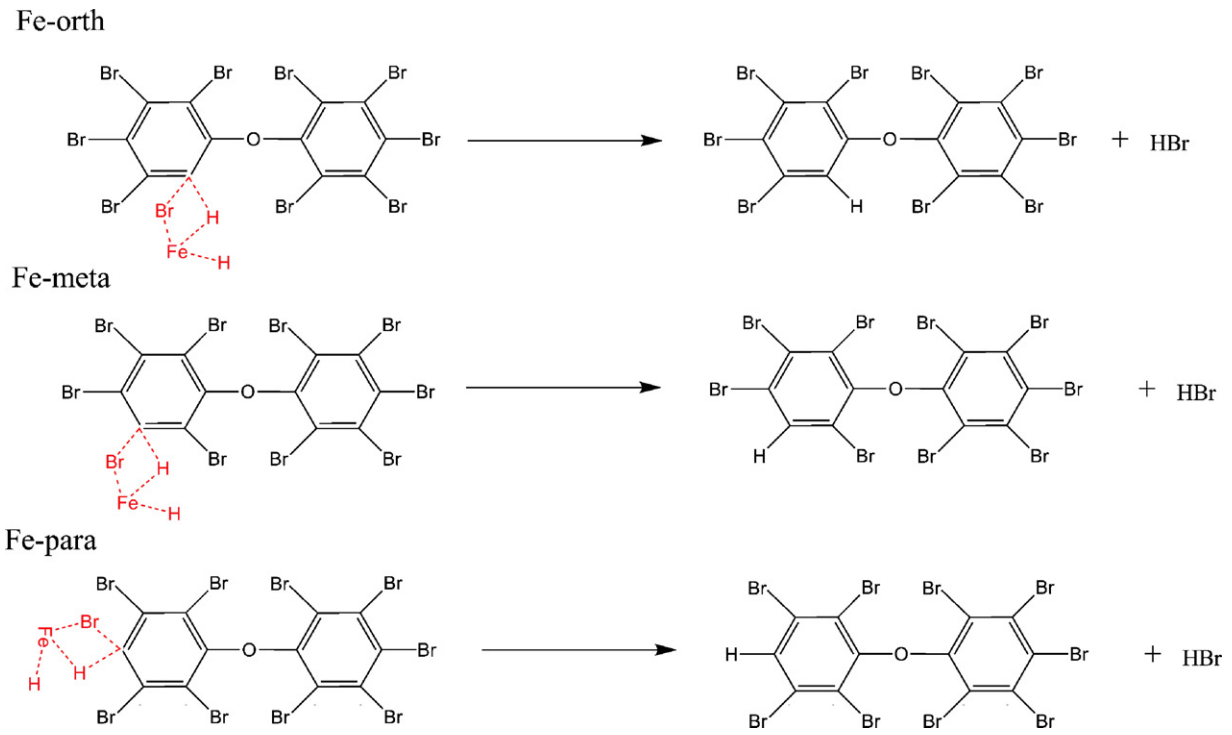

Fig. 13. Optimized transition state catalyzed by Fe.

degradation by SiO_2@FeOOH@Fe is shown in Fig. 12. For pure THF or a mixture of THF and EtOH, no BDE209 was removed. The proportion of water in the solvent was one of the important factors that influenced debromination efficiency. When the water content in the solution was increased, BDE209 degradation was notably enhanced. After 8 h, the degradation efficiency of BDE209 was only 32.73% in the THF/water (8/2, v/v) solution; the degradation rate increased to 52.59% in the THF/water (7/3, v/v) solution and then to 94.15% in the THF/water (6/4, v/v) solution. Catalytic hydrogenation was proposed by Shih and Tai [11] and Li et al. [29] as the major pathway for the debromination process based on their experimental data. The base reaction of dehalogenation by NZVI could be depicted by Eqs. (1)–(3).

$$Fe^0 \rightarrow Fe^{2+} + 2e^- \quad (1')$$

$$C_xH_yX_z + zH^+ + ze^- \rightarrow C_xH_{y+z} + zX^- \quad (2')$$

$$2Fe^{2+} + RX + H^+ \rightarrow 2Fe^{3+} + RH^+X^- \quad (3')$$

The reactions show that the presence of hydrogen ions in the solvent plays the most important role in the degradation of BDE209. The ionization constants (K_a) of the different solvents used in the present paper followed this trend: water ($K_a = 1 \times 10^{-14}$) > EtOH ($K_a = 1 \times 10^{-30}$) > THF (aprotic solvent). This indicates that water can provide more hydrogen ions than other organic solvents for reduction. In an organic solvent system, the aprotic solvent is THF, and the system cannot provide hydrogen ions for the reaction. Although EtOH is a protic solvent like water, its ionization constants (K_a) is 10^{16} times smaller than that of water, so the solution could not provide enough protons for the reaction, resulting in slow or non-existent reactions.

Meanwhile, quantum chemistry was adopted to study the effect of different mixed solvent on the degradation of BDE209 by nano

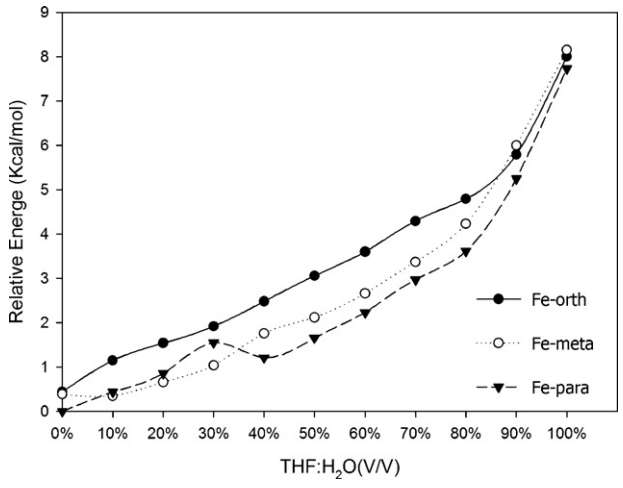

Fig. 14. Relative energies of optimized complex of metal Fe with BDE209 in different solvent.

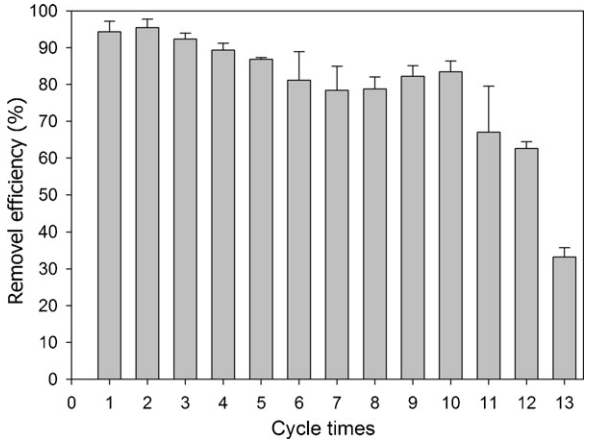

Fig. 15. Stability and durability of SiO_2@FeOOH@Fe in BDE 209 degradation. (SiO_2@FeOOH@Fe addition, 22 g L^{-1}, Fe loading of SiO_2@FeOOH@Fe was 18.01 wt%; initial concentration of BDE209, 1 mg L^{-1}; reaction time, 8 h; temperature, 28 ± 2 °C; pH 6.09.)

zero-valence iron further. All the calculations had been performed with the Gaussian 03 software package [53]. Molecular geometries were fully optimized at the Becke3LYP level of density functional theory [54–56]. What can be found is that besides providing hydrogen ion, the solvent has other impacts on degradation as follows. The first debromination of BDE209 by nano zero-valence iron shall form the following transition state (Fig. 13). This formation requires certain energy. The energy needed to form a transition state varied with different solvent and its water content. The following results are achieved by calculation. As we can see from the Fig. 14, with the decrease of water content, the energy needed increases constantly, which resulted in the slowdown of the reaction rate. This means that the reaction can be happed in the polar solvent condition more easier because the needed energies of forming transition state is less in the polar solvent. So the role of water is mainly not only to provide atomic hydrogen for the debromination, but also acts as a favorable composition of solvent for the debromination.

3.7. Stability and durability of SiO_2@FeOOH@Fe

To study the long-term degradation usability and stability of SiO_2@FeOOH@Fe for BDE209 degradation, 0.22 g of SiO_2@FeOOH@Fe and 10 mL of a 1 mg L^{-1} BDE209 solution were added to a 10 mL tube. The test tubes were sealed with a polytetrafluoroethylene plug, placed in an oscillator, and then agitated at a speed of 200 rpm. After one 8 h cycle, magnetic separation was used to separate the solution and particles, and all of the supernatant was removed, leaving the nanoparticles in the tube. Another 10 mL of the 1 mg L^{-1} BDE209 solution were added to the nanoparticles for one more cycle of degradation. The supernatant was filtered using a 0.45 μm microporous membrane. The concentration of BDE209 was measured by HPLC, and the results are shown in Fig. 15.

From the first five cycles, the degradation rate of 22 g L^{-1} SiO_2@FeOOH@Fe for 2 mg L^{-1} BDE209 reached higher than 85% (Fig. 9). In the sixth cycle, the degradation rate dropped to 81.15%. In the seventh to tenth cycles, the degradation efficiency of SiO_2@FeOOH@Fe for BDE209 slightly declined, although it remained within 78% to 83%. Its performance began to decline significantly from the 11th cycle and even dropped to 33.21% in the 13th cycle. This may be due to the erosion of NZVI particles on the surface of SiO_2@FeOOH@Fe by water, leading to form oxidizing layer and a loss of reaction sites during continuous degradation. This can be determined by the XPS spectrums of SiO_2@FeOOH@Fe before and after reaction. As shown in the Fig. 16, it is clearly found that two peaks at the binding energies of 706.9 eV and 710.8 eV existed in the XPS spectra of Fe (2p) before reaction. Peak at 706.9 eV demonstrated the existence of NZVI, while broad peaks at 710.8 eV was attributed to iron oxides (α-Fe_2O_3). But for the XPS spectra of Fe (2p) after reaction, peak at 706.9 eV was disappeared and the 710.8 eV still exist. This means that the iron oxide was generated on the surface of particles during the reaction.

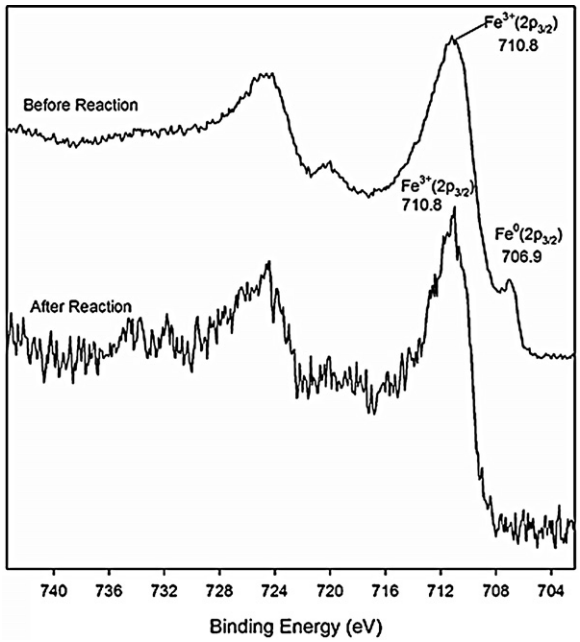

Fig. 16. XPS spectrum for the narrow scan of Fe 2p on the surface of SiO_2@FeOOH@Fe. (a) Narrow scan of Fe 2p before reaction; (b) narrow scan of Fe 2p after reaction.

3.8. Anti-agglomeration and magnetic separation of SiO_2@FeOOH@Fe

To study agglomeration after prolonged storage, similar amounts of SiO_2@FeOOH@Fe and NZVI were placed inside a flask filled with EtOH. The flasks were then sealed and stored at room temperature. A month later, the morphologies of these two materials were obtained, as shown in Fig. 17. After one-month storage, NZVI apparently clustered and formed a block structure (Fig. 17a). SiO_2@FeOOH@Fe remained in almost the same condition (Fig. 17b), and the particles were dispersed evenly in the solution. This demonstrates the improved anti-agglomeration ability of SiO_2@FeOOH@Fe, which is due to the presence of carriers in the particles. These carriers provide steric hindrance and weaken the agglomeration caused by the surface energy and magnetism between the nanoscale Fe particles.

SiO_2@FeOOH@Fe has anti-glomeration properties and can be recovered by magnetism. Its magnetic hysteresis loop showed that its saturant magnetic induction (M_s), coercive force, and magnetization ratio (M_r/M_s, where M_r is the magnetic remanence) were 33.979 emu g^{-1}, 235.97 G, and 0.18, respectively (Fig. 18a). This shows that SiO_2@FeOOH@Fe has ferromagnetic properties. When SiO_2@FeOOH@Fe particles were dispersed in an EtOH solution under an external magnetic field, the particles and solution were

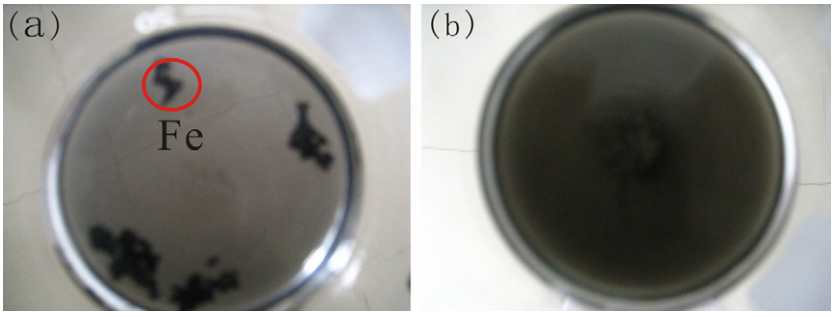

Fig. 17. Visual photos of (a) NZVI and (b) SiO_2@FeOOH@Fe after one month stored.

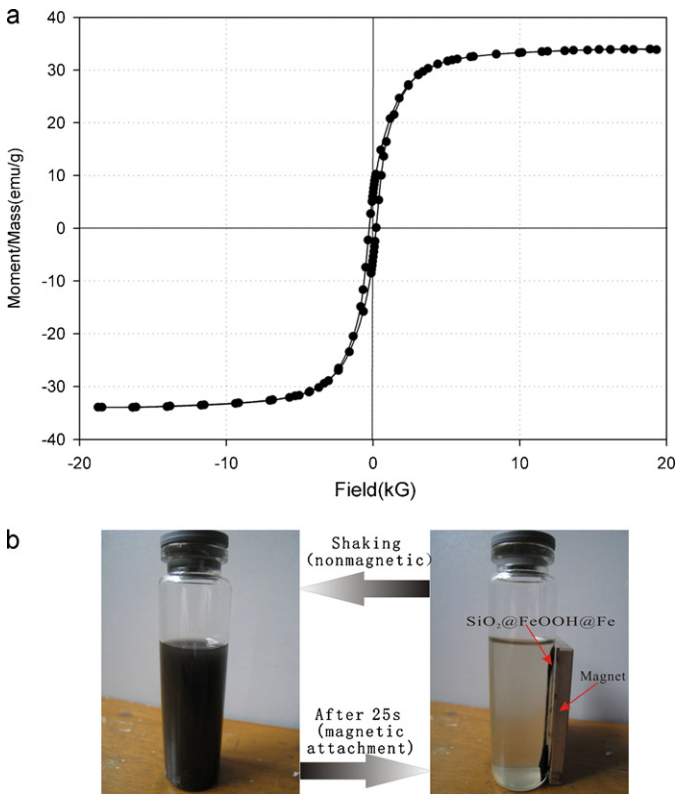

Fig. 18. (a) Magnetic hysteresis loop of SiO_2@FeOOH@Fe. (b) The separation–edispersion process of SiO_2@FeOOH@Fe.

fully separated after only 25 s (Fig. 18b). This shows the effective magnetic separation ability of SiO_2@FeOOH@Fe.

4. Conclusion

In the present study, we demonstrated a new approach for the immobilization of NZVI in mesoporous silica microspheres to enhance the dispersion of NZVI. Results from batch studies demonstrate that nanoscale SiO_2@FeOOH@Fe is effective in removing BDE209 from a THF/water solution at ambient temperature and pressure. The degradation of BDE209 follows a pseudo-first order kinetics model and the degradation efficiency of BDE209 benefits from an increased amount of SiO_2@FeOOH@Fe, resulting in a decrease in pollution levels. Through the reduction of BDE209 in different solvent condition and calculated the data by quantum chemistry, it strongly recommend that debromination is more effective in more water content due to hydrion was the driving forces of reaction and the energy needed to form transition state is less in polar solution. Comparing its degradation efficiency with that of NZVI and SiO_2@Fe under the same conditions, the degradation of BDE209 by SiO_2@FeOOH@Fe is more efficient. In addition, SiO_2@FeOOH@Fe also shows potential practicality for its stable degradation within 10 cycles and better performance in agglomeration-resistance and separation. The results obtained in this study clearly show that immobilized Fe nanoparticles in mesoporous silica microspheres can be practically and efficiently used for removing BDE209.

Acknowledgments

The authors are grateful for the financial support provided by the National Science and Technology Major Projects of Water Pollution Control and Management of China (2009ZX07011).

Appendix A. Supplementary data

Supplementary data associated with this article can be found, in the online version, at doi:10.1016/j.jhazmat.2011.07.024.

References

[1] X.Z. Peng, C.M. Tang, Y.Y. Yu, J.H. Tan, Q.X. Huang, J.P. Wu, S.J. Chen, B.X. Mai, Concentrations, transport, fate, and releases of polybrominated diphenyl ethers in sewage treatment plants in the Pearl River Delta, South China , Environ. Int. 35 (2009) 303–309.
[2] T. Shi, S.J. Chen, X.J. Luo, X.L. Zhang, C.M. Tang, Y. Luo, Y.J. Ma, J.P. Wu, X.Z. Peng, B.X. Mai, Occurrence of brominated flame retardants other than polybrominated diphenyl ethers in environmental and biota samples from southern China , Chemosphere 74 (2009) 910–916.
[3] P. Lindberg, U. Sellstrom, L. Haggberg, C.A. de Wit, Higher, Brominated diphenyl ethers and hexabromocyclododecane found in eggs of peregrine falcons (*Falco peregrinus*) breeding in Sweden , Environ. Sci. Technol. 38 (2004) 93–96.
[4] E. Eljarrat, A. de la Cal, D. Raldua, C. Duran, D. Barcelo, Occurrence and bioavailability of polybrominated diphenyl ethers and Hexabromocyclododecane in sediment and fish from the Cinca River, a tributary of the Ebro River (Spain) , Environ. Sci. Technol. 38 (2004) 2603–2608.
[5] X.J. Luo, B.X. Mai, S.J. Chen, Advances on study of polybrominated diphenyl ethers , Prog. Chem. 21 (2009) 359–368.
[6] P.A. Behnisch, K. Hosoe, S. Sakai, Brominated dioxin-like compounds: in vitro assessment in comparison to classical dioxin-like compounds and other polyaromatic compounds , Environ. Int. 29 (2003) 861–877.
[7] Y.T. Wei, S.C. Wu, C.M. Chou, C.H. Che, S.M. Tsai, H.L. Lien, Influence of nanoscale zero-valent iron on geochemical properties of groundwater and vinyl chloride degradation: a field case study , Water Res. 44 (2010) 131–140.
[8] L. Li, M.H. Fan, R.C. Brown, J.H.V. Leeuwen, J.J. Wang, W.H. Wang, Y.S. Song, P.Y. Zhang, Synthesis, properties, and environmental applications of nanoscale iron-based materials: a review , Crit. Rev. Environ. Sci. Technol. 36 (2006) 405–431.
[9] Z.Q. Fang, Q.X. Qiu, J.H. Chen, X.H. Qiu, Degradation of metronidazole by nanoscale zero-valent metal prepared from steel pickling waste liquor , Appl. Catal. B 100 (2010) 221–228.
[10] C.B. Wang, W.X. Zhang, Synthesizing nanoscale iron particles for rapid and complete dechlorination of TCE and PCBs , Environ. Sci. Technol. 31 (1997) 2154–2156.
[11] Y.H. Shih, Y.T. Tai, Reaction of decabrominated diphenyl ether by zero valent iron nanoparticles , Chemosphere 78 (2010) 1200–1206.
[12] B.W. Zhu, T. Lim, J. Feng, Reductive dechlorination of 1,2,4-trichlorobenzene with palladized nanoscale Fe^0 particles supported on chitosan and silica , Chemosphere 65 (2006) 1137–1145.
[13] F. Liang, J. Fan, Y.H. Guo, M.H. Fan, J.J. Wang, H.Q. Yang, Reduction of nitrite by ultrasound-dispersed nanoscale zero-valent iron particles , Ind. Eng. Chem. Res. 47 (2008) 8550–8554.
[14] A.B.M. Giasuddin, S.R. Kanel, H. Choi, Adsorption of humic acid onto nanoscale zero valent iron and its effect on arsenic removal , Environ. Sci. Technol. 41 (2007) 2022–2027.
[15] D.W. Elliott, H.L. Lien, W.X. Zhang, Degradation of Lindane by zero-valent iron nanoparticles , J. Environ. Eng. 135 (2009) 317–324.
[16] H.Y. Shu, C.M. Chang, H.H. Yu, W.H. Chen, Reduction of an azo dye acid black 24 solution using synthesized nanoscale zero valent iron particles , J. Colloid Interface Sci. 314 (2007) 87–89.
[17] Z.Q. Fang, X.H. Qiu, J.H. Chen, X.Q. Qiu, Degradation of the polybrominated diphenyl ethers by nanoscale zero-valent metallic particles prepared from steel pickling waste liquor , Desalination 267 (2011) 34–41.
[18] F. He, D.Y. Zhao, C. Paul, Field assessment of carboxymethyl cellulose stabilized iron nanoparticles for in situ destruction of chlorinated solvents in source zones , Water Res. 44 (2010) 2360–2370.
[19] J.J. Zhan, T.H. Zheng, G. Piringer, C. Day, G.L. McPherson, Y.F. Lu, K. Papadopoulos, V.T. John, Transport characteristics of nanoscale functional zero valent iron/silica composites for in situ remediation of trichloroethylene , Environ. Sci. Technol. 42 (2008) 8871–8876.
[20] G.K. Parshetti, R.A. Doong, Dechlorination of trichloroethylene by Ni/Fe nanoparticles immobilized in PEG/PVDF and PEG/nylon 66 membranes , Water Res. 43 (2009) 3086–3094.
[21] L. Alidokht, A.R. Khataee, A. Reyhanitabar, S. Oustan, Reductive removal of Cr(VI) by starch-stabilized Fe^0 nanoparticles in aqueous solution , Desalination 270 (2011) 105–110.
[22] X.H. Qiu, Z.Q. Fang, Degradation of halogenated organic compounds by modified nano zero-valent iron , Prog. Chem. 22 (2010) 291–297.
[23] F. He, D.Y. Zhao, J.C. Liu, C.B. Roberts, Stabilization of Fe-Pd nanoparticles with sodium carboxymethyl cellulose for enhanced transport and dechlorination of trichloroethylene in soil and groundwater , Ind. Eng. Chem. Res. 46 (2007) 29–34.
[24] F. He, D.Y. Zhao, Preparation and characterization of a new class of starch-stabilized bimetallic nanoparticles for degradation of chlorinated hydrocarbons in water , Environ. Sci. Technol. 39 (2005) 3314–3320.
[25] L.F. Wu, S.M. Ritchie, Removal of trichloroethylene from water by c ellulose acetate supported bimetallic Ni/Fe nanoparticles , Chemosphere 63 (2006) 285–292.

[26] H. Choi, S. Agarwal, S.R. Al-Abed, Adsorption and simultaneous dechlorination of PCBs on GAC/Fe/Pd: mechanistic aspects and reactive capping barrier concept , Environ. Sci. Technol. 43 (2009) 488–493.
[27] H. Choi, S.R. Al-Abed, S. Agarwal, D.D. Dionysiou, Synthesis of reactive Nano-Fe/Pd bimetallic system-impregnated activated carbon for the simultaneous adsorption and dechlorination of PCBs , Chem. Mater. 20 (2008) 3649–3655.
[28] X. Wang, C. Chen, H. Liu, J. Ma, Preparation and characterization of PAA/PVDF membrane-immobilized Pd/Fe nanoparticles for dechlorination of trichloroacetic acid , Water Res. 42 (2008) 4656–4664.
[29] A. Li, C. Tai, Z.S. Zhao, Y.W. Wang, Q.H. Zhang, G.B. Jiang, J.T. Hu, Debromination of decabrominated diphenyl ether by resin-bound iron nanoparticles , Environ. Sci. Technol. 41 (2007) 6841–6846.
[30] R. Saad, S. Thiboutot, G. Ampleman, W. Dashan, J. Hawari, Degradation of trinitroglycerin (TNG) using zero-valent iron nanoparticles/nanosilica SBA-15 composite (ZVINs/SBA-15) , Chemosphere 81 (2010) 853–858.
[31] Y. Ren, M. Chen, Y. Zhang, L.M. Wu, Fabrication of rattle-type TiO_2/SiO_2 core/shell particles with both high photoactivity and UV-shielding property , Langmuir 26 (2010) 11391–11396.
[32] Q.H. He, Z.X. Zhang, J.W. Xiong, Y.Y. Xiong, H. Xiao, A novel biomaterial—Fe_3O_4:TiO_2 core–shell nano particle with magnetic performance and high visible light photocatalytic activity , Opt. Mater. 31 (2008) 380–384.
[33] J.H. Ji, P.H. Zeng, S.H. Ji, W. Yang, H.F. Liu, Y.Y. Li, Catalytic activity of core–shell structured $Cu/Fe_3O_4@SiO_2$ microsphere catalysts , Catal. Today 158 (2010) 305–309.
[34] Z.Y. Shen, L.Y. Li, Y. Li, C.C. Wang, Fabrication of hydroxyl group modified monodispersed hybrid silica particles and the h-SiO_2/TiO_2 core/shell microspheres as high performance photocatalyst for dye degradation , J. Colloid Interface Sci. 354 (2011) 196–201.
[35] Y. Miyake, M. Yosuke, E. Azechi, S. Araki, S. Tanaka, Preparation and adsorption properties of thiol-functionalized mesoporous silica microspheres , Ind. Eng. Chem. Res. 48 (2009) 938–943.
[36] A. Matsumoto, T. Sasaki, N. Nishimiya, K. Tsutsumi, Evaluation of the hydrophobic properties of mesoporous FSM-16 by means of adsorption calorimetry , Langmuir 17 (2001) 47–51.
[37] C.H. Lee, D.L. Sedlak, Enhanced formation of oxidants from bimetallic nickel-iron nanoparticles in the presence of oxygen , Environ. Sci. Technol. 42 (2008) 8528–8533.
[38] Y. Luo, X.J. Luo, Z. Lin, S.J. Chen, J. Liu, B.X. Mai, Z.Y. Yang, Polybrominated diphenyl ethers in road and farmland soils from an e-waste recycling region in Southern China: concentrations, source profiles, and potential dispersion and deposition , Sci. Total Environ. 407 (2009) 1105–1113.
[39] A.C. Gerecke, P.C. Hartmann, N.V. Heeb, H.E. Kohler, W. Giger, P. Schmid, M. Zennegg, M. Kohler, Anaerobic degradation of decabromodiphenyl ether , Environ. Sci. Technol. 39 (2005) 1078–1083.
[40] H.X. Zhao, F.F. Zhang, B.C. Qu, X.Y. Xue, X.M. Liang, Wet air co-oxidation of decabromodiphenyl ether (BDE209) and tetrahydrofuran , J. Hazard. Mater. 169 (2009) 1146–1149.
[41] J. Eriksson, N. Green, G. Marsh, A. Bergman, Photochemical decomposition of 15 polybrominated diphenyl ether congeners in methanol/water , Environ. Sci. Technol. 38 (2004) 3119–3125.
[42] C.Y. Sun, D. Zhao, C.C. Chen, W.H. Ma, J.C. Zhao, TiO_2-mediated photocatalytic debromination of decabromodiphenyl ether: kinetics and intermediates , Environ. Sci. Technol. 43 (2009) 157–162.
[43] Ç. Üzüma, T. Shahwan, A.E. Eroğlu, K.R. Hallam, T.B. Scott, I. Lieberwirth, Synthesis and characterization of kaolinite-supported zero-valent iron nanoparticles and their application for the removal of aqueous Cu^{2+} and Co^{2+} ions , Appl. Clay Sci. 43 (2009) 172–181.
[44] N. Efecan, T. Shahwan, A.E. Eroglu, I. Lieberwirth, Characterization of the uptake of aqueous Ni^{2+} ions on nanoparticles of zero-valent iron (nZVI) , Desalination 249 (2009) 1048–1054.
[45] Y. Wang, L.Y. Wang, J.G. Tang, B. Yang, Preparation and properties of PET–PEG–SiO_2 co-polymerized hybrid nanoblocks , J. Mater. Eng. 10 (2008) 101–105.
[46] S.M. Ponder, J.G. Darab, J. Bucher, D. Caulder, I. Craig, L. Davis, N. Edelstein, W. Lukens, H. Nitsche, L. Rao, D.K. Shuh, T.E. Mallouk, Surface chemistry and electrochemistry of supported zerovalent iron nanoparticles in the remediation of aqueous metal contaminants , Chem. Mater. 13 (2001) 479–486.
[47] S. Araki, H. Doi, Y. Sano, S. Tanaka, Y. Miyake, Preparation and CO_2 adsorption properties of aminopropyl-functionalized mesoporous silica microspheres , J. Colloid Interface Sci. 339 (2009) 382–389.
[48] W.X. Zhang, C. Wang, H.L. Lien, Treatment of chlorinated organic contaminants with nanoscale bimetallic particles , Catal. Today 40 (1998) 387–395.
[49] R. Cheng, J.L. Wang, W.X. Zhang, The research progress on degradation of halogenated organic compounds by nano iron , Prog. Chem. 18 (2006) 93–99.
[50] Y. Xu, W.X. Zhang, Subcolloidal Fe/Ag particles for reductive dehalogenation of chlorinated benzenes , Ind. Eng. Chem. Res. 39 (2000) 2238–2244.
[51] X. Zhang, Y.M. Lin, Z.L. Chen, 2,4,6-Trinitrotoluene reduction kinetics in aqueous solution using nanoscale zero-valent iron , J. Hazard. Mater. 165 (2009) 923–927.
[52] Z. Zhang, N. Cissoko, J.J. Wo, X.H. Xu, Factors influencing the dechlorination of 2,4-dichlorophenol by Ni–Fe nanoparticles in the presence of humic acid , J. Hazard. Mater. 165 (2009) 78–86.
[53] M.J. Frisch, et al., Gaussian 03, Revision E.01 , Gaussian, Inc., Wallingford CT, 2004.
[54] A.D. Becke, Density-functional thermochemistry. III. The role of exact exchange , J. Chem. Phys. 98 (1993) 5648–5652.
[55] B. Miehlich, A. Savin, H. Stoll, H. Preuss, Results obtained with the correlation energy density functionals of becke and Lee, Yang and Parr , Chem. Phys. Lett. 157 (1989) 200–206.
[56] C. Lee, W. Yang, G. Parr, Development of the Colle-Salvetti correlation-energy formula into a functional of the electron density , Phys. Rev. B 37 (1998) 785–789.